Hydrological constraints on the potential of enhanced geothermal systems in the ductile crust

Samuel Scott[1]*, Alina Yapparova[2], Philipp Weis[3] and Matthew Houde[4]

*Correspondence:
samuels@hi.is

[1] Institute of Earth Sciences, University of Iceland, Reykjavik, Iceland
[2] Institute of Geochemistry and Petrology, ETH Zurich, Zurich, Switzerland
[3] GFZ Potsdam German Research Center for Geosciences, Potsdam, Germany
[4] Quaise Energy, Cambridge, MA, USA

Abstract

Continental crust at temperatures > 400 °C and depths > 10–20 km normally deforms in a ductile manner, but can become brittle and permeable in response to changes in temperature or stress state induced by fluid injection. In this study, we quantify the theoretical power generation potential of an enhanced geothermal system (EGS) at 15–17 km depth using a numerical model considering the dynamic response of the rock to injection-induced pressurization and cooling. Our simulations suggest that an EGS circulating 80 kg s^{-1} of water through initially 425 °C hot rock can produce thermal energy at a rate of ~ 120 MWth (~ 20 MWe) for up to two decades. As the fluid temperature decreases (less than 400 °C), the corresponding thermal energy output decreases to around 40 MWth after a century of fluid circulation. However, exploiting these resources requires that temporal embrittlement of nominally ductile rock achieves bulk permeability values of ~ 10^{-15}–10^{-14} m^2 in a volume of rock with dimensions ~ 0.1 km^3, as lower permeabilities result in unreasonably high injection pressures and higher permeabilities accelerate thermal drawdown. After cooling of the reservoir, the model assumes that the rock behaves in a brittle manner, which may lead to decreased fluid pressures due to a lowering of thresholds for failure in a critically stressed crust. However, such an evolution may also increase the risk for short-circuiting of fluid pathways, as in regular EGS systems. Although our theoretical investigation sheds light on the roles of geologic and operational parameters, realizing the potential of the ductile crust as an energy source requires cost-effective deep drilling technology as well as further research describing rock behavior at elevated temperatures and pressures.

Keywords: Geothermal energy, Enhanced geothermal systems, Superhot rock, Rock permeability, Numerical modeling

Introduction

Utilization of geothermal fluids at temperatures in excess of the critical point for water could theoretically multiply power generation compared to conventional geothermal wells in volcanically active areas, due to higher fluid enthalpies and greater efficiency in the conversion of thermal energy to electric energy (Friðleifsson et al. 2014). While temperatures > 375 °C can be found at shallow depth in volcanically active areas,

temperature increases much more slowly with depth in continental crust outside of volcanically active areas, but rock at temperatures > 400 °C can be found at depths of > 10 km over vast areas of the continents, and at > 20 km depth over the entire planet. Current enhanced geothermal systems (EGS) are limited to brittle rock at shallow depths (< 5 km) and temperatures < 250 °C, but future improvements in deep drilling technology could enable access to ductile rock at depths of > 10–20 km and temperatures > 400 °C, which would greatly increase the EGS resource base. However, the natural permeability of rock at such depths is low (10^{-18}–10^{-16} m^2; Manning and Ingebritsen 1999; Ingebritsen and Manning 2010; Townend and Zoback 2000), and accessing the heat stored in very deep rock by fluid circulation would require increasing and maintaining sufficient rock permeability by several orders of magnitude greater than the 'natural' background permeability.

Fluid injection in the brittle upper crust forms and reactivates networks of shear and tension fractures (Armstead and Tester 1987; Tester et al. 2006; Kohl and Megel 2007; Taron and Elsworth 2010; McClure and Horne 2014; Norbeck et al. 2018). The observation that measured stresses are approximately equal to the stresses predicted using Coulomb frictional-failure theory indicates a state of near-failure equilibrium where the upper crust is near-critically stressed (Townend and Zoback 2000; Zoback and Townend 2001; Sibson 2017). While zones of enhanced permeability formed during stimulation may be large (up to ∼ 2 km^3 in volume; Garcia et al. 2016), flow between injection and production wells is often channeled along a few dominant planar faults (Brown et al. 1999; Vik et al. 2018; Gee et al. 2021). This thermal "short-circuiting" results in rapidly declining production temperatures since heat conduction through fracture walls is slow (Gringarten et al. 1975; Bödvarsson and Tsang 1982) and limits the ability of an EGS to recover the heat of the rock (Fox et al. 2013; Grant et al. 2014). EGS also face challenges related to induced seismicity. Transiently elevated fluid pressures associated with injection can trigger slip along pre-existing elongate planar faults in the critically stressed upper crust, leading to earthquakes (Kraft and Deichmann 2014; Grigoli et al. 2018).

In contrast, ductile rock exhibits distributed failure mechanisms, including microcracking and crystal plastic phenomena such as diffusion creep at lower differential stress levels than required for brittle faulting (Tullis and Yund 1977; Rutter 1986; Meyer et al. 2019). The temperature and pressure range of the brittle–ductile transition depends on the geothermal gradient, rock rheological properties and strain rate (Goetze and Evans 1979; Brace and Kohlstedt 1980; Kohlstedt et al. 1995), and for continental crust it is believed to occur at 10–20 km depth (Carter and Tsenn 1987; Scholz 1988; Behr and Platt 2014) and temperatures of 400 ± 100 °C (Violay et al. 2017). Presently, our ability to drill into the ductile crust using conventional methods is practically limited by the forces of friction and material wear on the drill bits used to mechanically pulverize crystalline rock, which increase at higher temperatures (Finger and Blankenship 2010; Macini and Mesini 1994) and lead to exponentially increasing costs with depths (Lukawski et al. 2014). Moreover, there are significant challenges in delivering the potentially very high required injection pressures downhole without causing damage to well casing (Dusseault et al. 2001). However, active investigations are currently underway to develop alternative ways to drill through crystalline rock using thermal spallation (Beentjes et al. 2019; Kant

Scott *et al. Geothermal Energy*   (2024) 12:10

Page 3 of 26

et al. 2017; Rossi et al. 2020; Holtzman et al. 2023), electro-impulse (Lehmann et al. 2017), plasma (Oglesvy et al. 2014; Kocis et al. 2015) or millimeter-wave (Oglesby et al. 2014; Houde et al. 2021; Zhang et al. 2023) technologies. If these future advancements in drilling and stimulation technology enable economic access to deeper and hotter rock in the ductile crust, this could create the potential for a new type of EGS resource, which we refer to in this paper as nominally ductile rock EGS (NDR-EGS).

The continental crust at temperatures > 400 °C is 'nominally ductile' as it can undergo temporary embrittlement in response to changes in stress, strain rate, temperature, and fluid pressure, leading to failure and potential permeability enhancement (Rutter 1986; Sibson 1983; Scholz 1988; Paterson and Wong 2005). This embrittlement of NDR is evidenced by deep earthquakes (Jackson 2002; Handy and Brun 2004; Ingebritsen and Manning 2010) and in the rock record, for instance in the form of stockwork veining in porphyry copper deposits (e.g., Sillitoe 2010), fault-valve behavior in orogenic gold deposits (e.g., Sibson et al. 1988), and cataclastic rocks originating from lower- to mid-crustal ductile shear zones (e.g., Wehrens et al. 2016). Experiments have demonstrated that failure of NDR leads to permeability enhancement of two orders of magnitude even in the absence of pore fluids (Jones et al. 1997; Meredith et al. 2012; Petrini et al. 2021). In addition to reducing the effective stress, making the rock more likely to fail, fluid injection into hot rock will trigger the volumetric contraction of the rock and thermal cracking (Jones et al. 1997; Tarasovs and Ghassemi 2014), which can increase permeability by up to four orders of magnitude (Wang et al. 2013; Siratovich et al. 2015). As permeability is distributed in a three-dimensional network of permeable microfractures throughout the rock mass (Watanabe et al. 2017, 2019, 2020; Goto et al. 2021, 2023) rather than planar faults, the much higher tortuosity of the formed fracture network may enhance heat extraction in NDR.

NDR-EGS have the potential to offer advantages over conventional EGS, such as higher production temperatures, enhanced fluid penetration into the rock mass, and simpler design and control of the reservoir owing to more uniform rock properties and the absence of pre-existing, critically stressed faults. However, in addition to the challenge of drilling to such depths, NDR-EGS also pose potential risks, including high injection pressures required to stimulate the rock, potential rapid permeability loss, casing failure due to ductility (Watanabe et al. 2020; Frost and Ashby 1977), high-temperature fluid–rock interactions (Moore et al. 1994), and the potential for induced seismicity (Parisio et al. 2019). Although the decrease in the amount of seismicity (Sibson 1983; Chen and Molnar 1983) and the transition to higher electrical conductivities (Haak and Hutton 1986) at lower crustal depths was once interpreted as indicating the widespread presence of trapped over-pressured fluids (Bailey 1990), more recent petrologic (Yardley and Valley 1997) as well as geophysical (Simpson 2001) arguments suggest that pore fluids are consumed by hydration reactions and the lower crust outside of orogenic terranes is essentially dry in the interiors of continental plates (Yardley 2009). The world's deepest boreholes, Kola and KTB, which were drilled to ~ 12 km and ~ 9 km depth, respectively, encountered maximum temperatures ~ 200 °C, near-hydrostatic pore pressures, and bulk permeability of 10^{-17}–10^{-16} m^2 (Kozlovsky 1987; Popov et al. 1999; Townend and Zoback 2000).

Computational modeling offers an avenue for quantifying the theoretical power generation potential of NDR-EGS. In this exploratory study, we present the first numerical simulations of such systems with hypothetical injectors and producers placed beneath the brittle–ductile transition in normal continental crust with an average geothermal gradient. Due to the absence of hard constraints from experiments and observations in the current literature, we treat the absolute permeability response of NDR to failure as uncertain and test the dependence of the system on different assumptions (e.g., maximum permeability in the stimulated volume after rock failure) and operational scenarios (e.g., well configuration and injection rate). The primary aim of these simulations is to clarify the bulk rock permeability range that would maximize the long-term power generation potential of an enhanced geothermal system in nominally ductile continental crust at ~ 15 km depth.

Methods

The simulations are performed using an implementation of the Complex Systems Modeling Platform (CSMP++; Matthäi et al. 2007) for multi-phase hydrothermal fluid flow (e.g., Weis et al. 2014). We further developed this simulator for our application to NDR-EGS by combining a well model enabling more realistic simulation of fluid production/injection around a wellbore (Yapparova et al. 2022, 2023) with a modification of a dynamic permeability model simulating hydraulic fracturing and the brittle–ductile transition (Weis et al. 2012).

Governing equations for fluid flow

The governing equations of multi-phase mass and energy conservation are solved using a continuum porous media approach with a pressure–enthalpy–salinity-based formulation in a Control Volume-Finite Element Method (CVFEM) numerical scheme, which has been described in detail by Weis et al. (2014).

Phase velocities of liquid (*l*) and vapor (*v*) are obtained using Darcy's law:

$$v_i = -\frac{k}{\mu_i}(\nabla p - \rho_i \boldsymbol{g}), \tag{1}$$

where k is the rock permeability, μ_i dynamic viscosity of fluid phase i ($i = l,v$), ∇p pressure gradient, ρ_i fluid phase density, and g the gravitational acceleration vector. The pore fluid consists of pure water and all fluid properties correspond to Haar et al. (1984). The simulator can handle fluid phase separation if two-phase conditions are reached. Because the modeled conditions of interest for NDR-EGS are above the pressure of the critical point of H_2O, the fluids (*f*) remain at supercritical single-phase conditions in our simulations and we simplify the equations accordingly for readability.

For single-phase conditions, conservation of fluid mass is given by:

$$\frac{\partial\left(\phi\rho_f\right)}{\partial t} = -\nabla \cdot \left(v_f \rho_f\right) + Q_{H_2O}, \tag{2}$$

where ϕ is rock porosity and Q_{H2O} is a fluid source term (representing fluid mass added or removed from the system from the injection/production wells). Energy conservation accounts for conduction of heat in the rock and advection of enthalpy by fluid:

Scott *et al. Geothermal Energy*   (2024) 12:10

Page 5 of 26

$$\frac{\partial\left((1-\phi)\rho_r h_r + \phi\rho_f h_f\right)}{\partial t} = \nabla \cdot (K\nabla T) - \nabla \cdot \left(v_f \rho_f h_f\right) + Q_a + Q_c, \tag{3}$$

with K as the thermal conductivity of the rock, $Q_a = Q_{H_2O} h_f$ as a source/sink term for the energy added or removed through the well fluids with the enthalpy of the fluid h_f at given temperature and pressure conditions, and Q_c as a source term for the heat flux across the bottom boundary which maintains the geothermal gradient. Fluid and rock are assumed to be in local thermal equilibrium, and total enthalpy is distributed over fluid and rock contained in a control volume such that they are at the same temperature (Weis et al. 2014).

Well model

The source/sink well model used with the CVFEM approach in CSMP++ is based on the approach of Peaceman (1978) as described in Yapparova et al. (2022, 2023). Peaceman's model is essentially a 2D model that assumes radial Darcy flow in a thin horizontal layer of thickness h in the near-vicinity of a well, with an analytical solution for pressure in the vicinity of the well given by:

$$p(r) = p_w - \frac{q\mu_i}{2\pi h\rho_f k}\ln\left(\frac{r}{r_w}\right), \tag{4}$$

where q is the source/sink term representing the well, p_w and r_w are the well pressure and the well radius, respectively, and r is the distance from the well.

In CSMP++, wells are 1D line element regions embedded in a 3D volumetric element mesh, and are represented as internal model boundaries. Wells are set up either with rate or pressure control, with injection/production rate or well pressure fixed at the well nodes, respectively (Yapparova et al. 2022). For each mesh node containing the well, two pressure variables (fluid pressure p and well pressure p_w) are used to account for the steep pressure gradients surrounding an injection/production well. For wells simulated using rate control, the specified injection/production rate affects the pressure equation in CVFEM through the mass source/sink term Q_{H_2O}, which can be formulated as:

$$\rho_f\left[\phi\beta_f + (1-\phi)\beta_r\right]\frac{\partial p}{\partial t} = \nabla \cdot \left(\frac{k\rho_f}{\mu_f}\nabla p\right) - \frac{k\rho_f^2}{\mu_f}\mathbf{g} + Q_{H_2O} + Q_p \tag{5}$$

for single-phase conditions, with β_f and β_r as the compressibility of fluid and rock, respectively, and a pressure source term Q_p for temperature-dependent changes in fluid density (for a derivation of the equation at multi-phase conditions see Weis et al. 2014). The mass source/sink term Q_{H_2O} is also considered in Eq. 2 and further used to calculate the energy source term Q_a in Eq. 3 by multiplication with the fluid enthalpy h_f for the current reservoir pressure and the prescribed temperature of the injected fluids (source at injection wells) or current calculated reservoir temperature at the well nodes (sink at production wells). For a given fluid source rate, we divide the additional fluid mass and energy for a modeling time step across the finite volumes representing the well in proportion to their respective sizes in the unstructured mesh.

The well pressure is then calculated using a modified version of Eq. (4):

$$p_w = p + \frac{Q_{H2O}\mu_f}{2\pi h \rho_f k}\ln\left(\frac{r}{r_w}\right). \tag{6}$$

For the injection intervals, we use this rate-controlled formulation and the well pressure is greater than the reservoir pressure surrounding the well.

We simulate the nodes comprising the production intervals under pressure control, where the well pressure is specified, and the unknown reservoir pressure appears in the source term in the pressure equation:

$$Q_{H2O} = \frac{2\pi h k \rho_f}{\mu_f[\ln\left(\frac{r_e}{r_w}\right) + S]}, \tag{7}$$

where r_e is the analog of the effective radius (Peaceman 1978) and S is the skin factor, accounting for either formation damage resulting from drilling (positive skin) or flow enhancement due to hydraulic fracturing or acid treatment of the well (negative skin). For a well under pressure control, the mass flow into or out of the well is the actual injection/production rate of a well given the fluid pressure at the well. For a production well, the well pressure is set to a value less than the reservoir pressure, representing the steady-state 'flowing' pressure at which fluid will flow into the well. Below this minimum, no fluid will flow into the well.

Dynamic permeability model

To simulate the dynamic permeability evolution during well operation, we modified a permeability model that has originally been compiled within CSMP++ from published permeability-related observations and conceptual models to mimic the formation of stockwork veining at porphyry copper deposits (Weis et al. 2012; Weis 2015) and has subsequently also been used with HYDROTHERM to investigate distal volcano-tectonic seismicity (Coulon et al. 2017). This model assumes that fluid pressures exceeding a critical failure pressure defined for brittle and ductile rock will lead to an increase in interconnected pore space and permeability after fracturing. By applying the linear Coulomb criterion for normal-faulting conditions, the failure pressure assuming optimally oriented brittle shear failure in intact rock with a coefficient of internal friction of 0.75 is given by (Cox 2010; Weis 2015):

$$p_{\text{fail}} = \sigma_v - \frac{4(\sigma_{\text{diff}} - C)}{3}, \tag{8}$$

where σ_v is the vertical stress (approximated by the lithostatic load and assumed to be equivalent to σ_1), C is the cohesive strength (10 MPa), and $\sigma_{\text{diff}} = \sigma_1 - \sigma_3$ is the differential stress. Failure pressures close to the hydrostatic pressure have been observed during deep drilling worldwide (Zoback and Harjes 1997; Townend and Zoback 2001) and support the hypothesis that critically stressed faults limit the strength of the crust (Zoback and Townend 2001; Sibson 2017). For brittle crust, we assumed that the failure pressure exceeds the calculated initial hydrostatic fluid pressure by 5 MPa (the assumed tensile strength of the rock).

We can then calculate a differential stress profile for brittle rock by rearranging Eq. 8:

$$\sigma_{\text{diff,brittle}} = \frac{3}{4}\left(\sigma_v - p_{\text{fail,brittle}}\right) + \frac{5}{8}C. \tag{9}$$

The differential stress at ductile rock conditions is calculated using the power-law creep relationship (Brace and Kohlstedt 1980):

$$\sigma_{\text{diff,ductile}} = \sqrt[n]{\frac{\dot{\varepsilon}}{A \cdot \exp\left(-Q/_{RT}\right)}}, \tag{10}$$

where $\dot{\varepsilon}$ is the strain rate, and Q, A, and n are rheological parameters the values of which were obtained for bulk upper crustal rocks (Zoback and Townend 2001; Zoback et al. 2002) and are listed in Table 1. In this study, we calculated $\sigma_{\text{diff,ductile}}$ using a constant strain rate of 10^{-15} s^{-1}, which is two to three orders of magnitude greater than average strain rates for the upper crust (Zoback and Townend 2001), reflecting the elevated strain rates likely to be present during injection. The failure pressure is then calculated using Eq. 8, based on the assumption that the rock deforms under the minimum differential stress calculated for brittle and ductile rock:

$$\sigma_{\text{diff}} = \min\left(\sigma_{\text{diff,brittle}}, \sigma_{\text{diff,ductile}}\right). \tag{11}$$

Thus, although the failure pressure given in Eq. (8) applies the linear Coulomb criterion for brittle shear failure, we can use this same failure criterion to define failure pressures in nominally ductile rock by substituting $\sigma_{\text{diff,ductile}}$ into Eq. (8). According to this model, as the differential stress in ductile rock relaxes to zero with increasing depth and temperature, failure pressure gradually increases up to the lithostatic value (Fig. 1d). When $\sigma_{\text{diff,ductile}} < \sigma_{\text{diff,brittle}}$, the background permeability is calculated using the temperature-dependent approach of Hayba and Ingebritsen (1997), using the depth-dependent permeability at the depth and temperature of the brittle–ductile transition (Fig. 1a).

The original permeability model of Weis et al. (2012) assumed fast permeability decay if fluid pressures decrease below the failure criterion after hydraulic fracturing, assuming efficient fracture healing during the formation of stockwork veins by quartz precipitation from high-temperature magmatic fluids. However, in the case of NDR-EGS systems, cold water is injected into hot rock which would lead to an increase in quartz solubility

Table 1 Values of petrophysical parameters assumed in model calculations

Property	Value
Rock porosity (ϕ)	0.01
Rock density (ρ_r)	2700 kg m^3
Thermal conductivity (λ)	Temperature-dependent according to Whittington et al. (2009)
Rock isobaric heat capacity ($c_{p,r}$)	880 J kg^{-1} C^{-1}
Rock compressibility (β_r)	5×10^{-10} Pa^{-1}
Stress exponent (n)[a]	3.1
Activation energy (Q)[a]	243 kJ mol^{-1}
Flow parameter (A)[a]	0.08

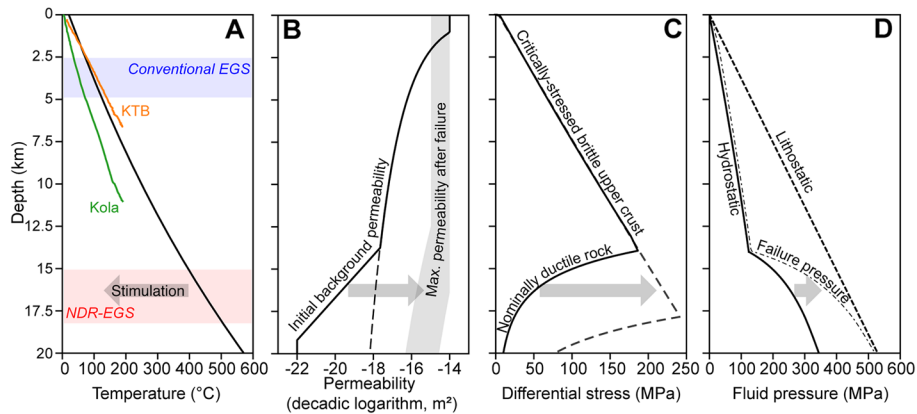[a] Representative value for upper crust from Zoback and Townend (2001)

Fig. 1 Model assumptions describing the structure of the upper continental crust. **A** Temperature–depth profiles assuming basal heat fluxes of 75 mW m^{-2}, and temperature-dependent thermal conductivity representative of bulk crustal materials (Whittington et al. 2009). Measured temperatures from Kola superdeep (Popov et al. 1999) and German Continental Deep Drilling Program KTB (Clauser et al. 1997) are shown with green and orange lines. **B** Permeability–depth profile. The solid black line shows the initial permeability, which is depth-dependent (Ingebritsen and Manning 1999) in brittle rock, and temperature-dependent (Hayba and Ingebritsen 1997; Scott et al 2015) in ductile rock. After failure, permeability increases by two to four orders of magnitude (grey area) above the background depth-dependent value, shown by the dashed line. **C** Differential stress profile assuming optimally oriented shear failure for compressive effective normal stress conditions in critically stressed crust (Sibson 2017), and power-law creep (Kohlstedt et al. 1995) at ductile conditions. **D** Fluid pressure, failure pressure (thin-dashed-dot) and lithostatic pressure (thick-dashed) with depth. Initial fluid pressure is hydrostatic in the brittle upper crust and over-pressured in the ductile regime. In the upper crust, rock fails with small overpressure values corresponding to the tensile strength of the rock (Cox 2010); in the ductile crust, our model assumes that failure pressure increases as the differential stress relaxes. The grey arrows show the variations of properties during rock stimulation, including cooling by fluid injection (**A**), permeability enhancement (**B**), rock embrittlement (**C**), and pressurization (**D**)

as well as thermal stress cracking. For this study, we therefore assume that elevated fluid pressures can maintain interconnected pore space and fracture networks after stimulation, even if they have decreased below the failure pressure. This assumption also infers that potential ductile deformation, which may also lead to permeability decay but is not resolved by our model, is subordinate to the processes considered in this model.

We assume that permeability decay has a log-quadratic dependence on the modified pore fluid factor ($\lambda = \frac{p_{\text{fluid}}}{p_{\text{fail}}}$; Weis et al. 2012; Weis 2015). The modified pore fluid factor is normalized to values between 0–1 by assuming that a hydrostatic fluid pressure corresponds to a modified pore fluid factor of 0 and $p_{\text{fluid}} \leq p_{\text{fail}}$. Then, at fluid pressures intermediate between the failure pressure and the initial ('hydrostatic') pressure, permeability is calculated as:

$$\log_{10}(k) = \log_{10}(k_{\max})\lambda^2 + (1 - \lambda^2)\log_{10}(k_{\text{bkg}}), \tag{12}$$

where $k_{\max}$ is the maximum permeability and k_{bkg} is the background permeability. Where $\sigma_{\text{diff,ductile}} < \sigma_{\text{diff,brittle}}$, k_{bkg} is calculated using the log-linear temperature-dependent approach initially introduced by Hayba and Ingebritsen (1997):

$$\log_{10}\left(k_{\text{bkg,ductile}}\right) = \frac{\log_{10}(k_{\min})(T - T_{\text{onset}}) + \log_{10}(k_{\text{onset}})(T_{\text{end}} - T)}{(T_{\text{end}} - T_{\text{onset}})}. \tag{13}$$

In this study, T_{onset} and k_{onset} reflect the temperature and permeability conditions at the onset of the brittle–ductile transition (i.e., where $\sigma_{\text{diff,brittle}} = \sigma_{\text{diff,ductile}}$) and T_{end} and k_{min} (assumed to be 550 °C and 10^{-22} m^2 in this study). At brittle conditions, the background permeability is calculated using the depth-dependent formulation of Manning and Ingebritsen (1999):

$$\log_{10}\left(k_{\text{bkg,brittle}}\right) = -3.2\log_{10}(z) - \log_{10}\left(k_{\text{bkg,ref}}\right), \tag{14}$$

where z is in km and $k_{\text{bkg,ref}}$ is assumed to be 10^{-14} m^2 for average continental crust at 1 km depth. The maximum permeability uses the same type of equation:

$$\log_{10}\left(k_{\text{bkg,brittle}}\right) = -3.2\log_{10}(z) - \log_{10}\left(k_{\text{bkg,max}}\right), \tag{15}$$

with $k_{\text{bkg,max}}$ being 2–4 orders of magnitude higher than $k_{\text{bkg,ref}}$, depending on the model configuration.

Figure 2 shows the relationship between permeability and fluid pressure for ductile (Fig. 2a) and brittle (Fig. 2b) rock at 15 km and 17 km depth, according to our dynamic permeability model and the initial conditions considered in this study. Increasing permeability by two to four orders of magnitude relative to the depth-dependent value ($\sim 10^{-18}$ m^2) corresponds to maximum permeability of $\sim 10^{-16}$ m^2, $\sim 10^{-15}$ m^2, or $\sim 10^{-14}$ m^2, as shown by the blue, black and red lines, respectively. The vertical dashed lines labeled $p_{fail,ductile}$ indicate that the failure pressure for ductile rock ranges between ~ 350 and 450 MPa over this depth range, approaching lithostatic at 17 km depth. Permeability does not increase further with increasing fluid pressure above the ductile failure criterion, and there is a log-quadratic relationship between pore fluid factor and permeability at fluid pressures intermediate between the hydrostatic fluid pressure and failure pressure, as defined by Eq. (12). If maximum permeability is $\sim 10^{-14}$ m^2 (red lines in Fig. 2a), fluid pressures > 300 MPa and > 400 MPa are required to maintain permeability $> 10^{-16}$ m^2 in ductile rock. In contrast, brittle
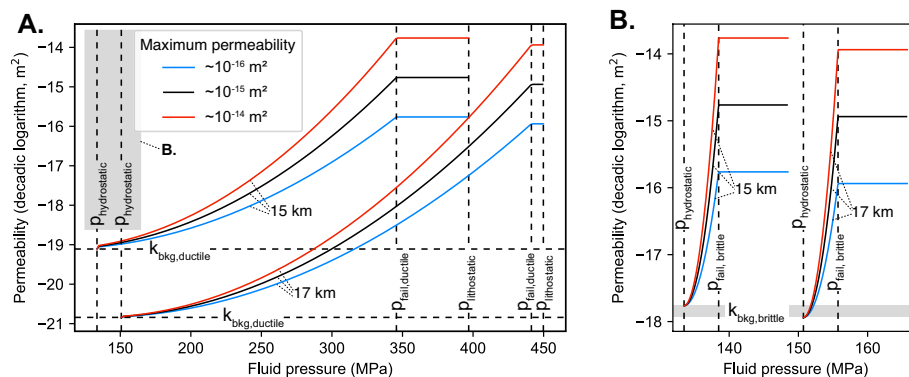

Fig. 2 Relationship between permeability and fluid pressure for **A** ductile and **B** brittle rock at 15 and 17 km depth. In **A**, the vertical dashed lines represent hydrostatic fluid pressure ($p_{\text{hydrostatic}}$), ductile failure pressure ($p_{\text{fail,ductile}}$), and lithostatic pressure ($p_{\text{lithostatic}}$), and the horizontal dashed lines background permeability in ductile rock ($k_{\text{bkg,ductile}}$). The grey region in **A** shows the area expanded in **B**. In **B**, the vertical dashed lines represent the hydrostatic fluid pressure and the brittle failure pressure ($p_{\text{fail,brittle}}$), with the grey region showing background depth-dependent permeability in brittle rock ($k_{\text{bkg,brittle}}$). In our models, permeability increases by two to four orders of magnitude relative to the depth-dependent value, resulting in maximum permeability of about 10^{-16} m^2 (blue lines), 10^{-15} m^2 (black lines), or 10^{-14} m^2 (red lines)

rock fails at fluid pressures only slightly more than the initial hydrostatic value. If fluid pressure drops below the failure pressure in brittle rock, permeability rapidly approaches the depth-dependent value according to a similar log-quadratic relationship.

This parameterization mimics a pressure- and temperature-dependent dynamic rock behavior between brittle and ductile in a simplified form using a continuum porous medium formulation. Although we use some available constraints from the literature, additional complexities such as poroelasticity, thermal and/or reaction-driven cracking, and explicit fracture growth are not yet considered in this model. In that sense, our modeling should be considered as a first reconnaissance study. Once the processes and properties relevant for these types of systems can be further constrained with new experimental studies, the numerical model can be adapted accordingly.

Model set-up

A typical model configuration is shown in Fig. 3. The 3-dimensional computational domain is 15 km × 15 km × 15 km in extent, consisting of roughly 28,000 elements. The resolution of the elements increases in the vicinity of the wells, which are modeled as a series of 1-dimensional line elements embedded in the tetrahedral mesh. Initially, the porous medium is saturated with water and thermally equilibrates with a basal heat flux, which is set to 75 mW m^{-2}. Assumed values for petrophysical properties used in model calculations are listed in Table 1.

The top boundary is fixed at the hydrostatic fluid pressure and steady-state temperature at 6 km depth. As shown in Fig. 3, the resolution of the finite element mesh dramatically increases in the vicinity of the wells, as the maximum resolution (length) of the 1-D line elements constituting the wells was set to 50 m. The bottom boundary assumes a no-flow condition, while the side boundaries assume a constant (hydrostatic)
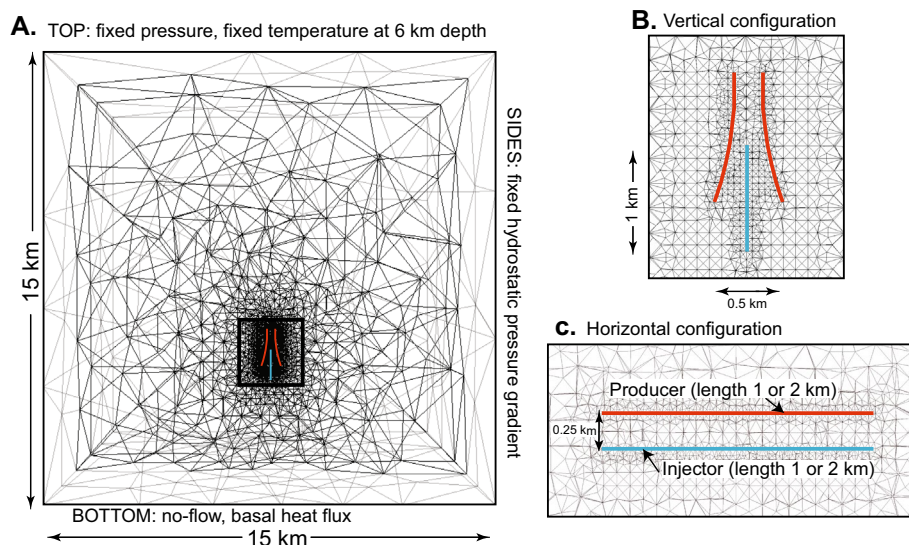

Fig. 3 Example model set-up and finite element discretization. **a** Vertical slice over entire domain along plane through wells (injection well shown in blue, production wells in red). **b** Vertical slice showing area around vertical wells in more detail. **c** Vertical slice showing horizontal well configuration. For this study, the length of the production and injection intervals was set to 1 km

pressure gradient. To investigate the effect of this assumption, simulations considering a no-flow boundary condition for the side boundaries were also performed. However, no significant differences between simulations with constant pressure gradient or no-flow side boundary conditions were observed, indicating that the evolution of fluid pressures in the vicinity of the wells was controlled by the permeability of the surrounding rock, rather than the boundary conditions.

Figure 3b illustrates a vertical triplet well configuration, featuring an injection interval located at a depth of 16–17 km. Two directionally oriented production intervals begin at 15.5 km depth and transition to a more lateral orientation at 15.75 km depth, characterized by a kick-off angle of 10° and azimuth of 90° relative to the injector. This particular geometric arrangement was selected based on testing results that demonstrated that production intervals positioned near and partially above the injector effectively depressurize the stimulated volume. Additionally, the directional aspect of the production intervals enhances the size of the stimulated volume, particularly at long timescales, in contrast to configurations with vertically straight production intervals. Figure 3c shows a horizontal oriented system with a spacing of 0.25 km depth. While tests indicate that variable well spacing can modulate the rate of temperature decline in the stimulated volume, this study discusses results from the configurations depicted in Fig. 3b and c.

Results

Modeled hydrology with well triplet

Our computational models simulate the dynamic evolution of nominally ductile rock enhanced geothermal systems (NDR-EGS) during transient embrittlement and consequent permeability enhancement induced by fluid injection. Figure 4 shows the modeled fluid pressure distribution around vertically oriented wells arranged in a 'triplet' configuration, with a centrally located injection interval at 16–17 km depth (blue line, Fig. 4) flanked by production intervals at 15.5–16.5 km depth (red lines). In this simulation, we permit a permeability increase by three orders of magnitude compared to the initial depth-dependent value, leading to a maximum absolute permeability value of about
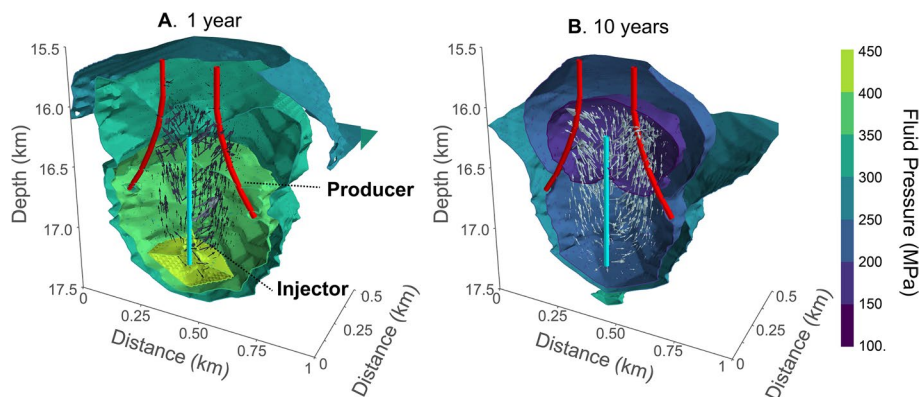

Fig. 4 Three-dimensional structure of a nominally ductile rock enhanced geothermal system (NDR-EGS) showing the fluid pressure distribution around a geothermal triplet, with a centrally located injector (blue) located between two production intervals (red). Results are shown after **A** 1 year and **B** 10 years for a simulation with an injection rate of 80 kg s^{-1} and a maximum permeability of ~ 10^{-15} m^2

10^{-15} m^2. The extent of the potential geothermal reservoir within the boundaries of the stimulated volume corresponds to the vector field of fluid flow in Fig. 4. Fluid flows through a stimulated volume (SV) that extends from the injector to the producers. In this study, the SV is defined as rock with permeability $> 10^{-16}$ m^2, which likely delineates a lower bound necessary for an exploitable geothermal resource since heat transfer is conduction-dominated below this threshold (Ingebritsen et al. 2006), as also illustrated by the lack of visible flow vectors surrounding the SV in Fig. 4.

The simulations reveal how fluid flow self-organizes in response to a dynamic relationship between fluid pressure, permeability, and ductile rock behavior (Fig. 1) that controls the long-term behavior of NDR-EGS. After one year of operation (Fig. 4a), fluid pressures close to the failure pressure of the rock (350–400 MPa) develop between the injector and producers. Establishing a hydraulic connection sufficient to support advective heat transport between the injector and producer is of critical importance during this stage, because otherwise the pressure anomaly induced by fluid injection progresses into the overlying brittle crust, which may trigger seismicity due to the lower failure criterion (Fig. 1d) under critically stressed conditions (Fig. 1c). After this hydraulic connection has been established, continued injection cools the SV, which leads to increasingly brittle rock behavior (grey arrow in Fig. 1c) and a reduction in failure pressure closer to the hydrostatic pressure gradient, assuming that critically stressed conditions also apply at these temperatures and depths (Fig. 1d). Once the SV cools below the brittle–ductile transition temperature, the SV retains permeability at lower fluid pressures, enabling fluid flow through the SV at pressures well below the failure pressure of surrounding ductile rock at longer timescales (Fig. 4b), thereby limiting the risk of unwanted rock stimulation and induced seismicity outside of the SV.

The influence of well configuration and permeability in the stimulated volume

The size and orientation of the stimulated volume controls the efficiency and longevity of NDR-EGS. Figure 5 shows the simulated temperature distribution around NDR-EGS
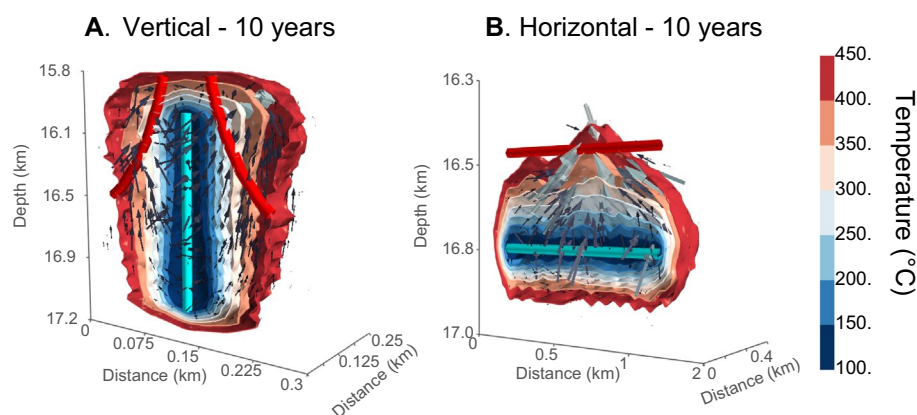

Fig. 5 The temperature distribution around a NDR-EGS after 10 years of fluid circulation. Results are shown for 3D model cut-outs with **A** vertically and **B** horizontally oriented production and injection intervals, for simulations with an injection rate of 80 kg s^{-1} and a maximum permeability in the stimulated volume of $\sim 10^{-15}$ m^2

with vertically (Fig. 5a) or horizontally oriented (Fig. 5b) production and injection intervals. Around vertical injection intervals, fluid injected at depth beneath the production interval(s) mines heat from the deeper rocks, ascends through a relatively narrow (~0.25 km) SV, and flows laterally into the production interval at ~16 km depth, close to where the distance between the injector and producer is minimized (~0.15 km). If the injection and production intervals are horizontal (Fig. 5b), the injected fluid flows through a more laterally extensive SV and into an overlying production interval through a ~0.2 km wide zone with lower temperatures than the surrounding rock. Thus, although both vertically and horizontally oriented configurations show a tendency for production temperatures to decrease due to flow channeling into the coolest areas, maintaining a vertically extensive and/or broad SV enables heat extraction from a larger volume of rock and slows the rate of temperature decrease at the production wells. For example, after 10 years of fluid circulation, the temperature of fluid flowing into the production intervals is above 300 ℃ for a vertically oriented system and above 350 ℃ for a horizontally oriented system (Fig. 5).

Higher permeability in the SV allows the production intervals to depressurize the SV more effectively, resulting in a smaller SV that is more confined to the vicinity of the injector. Figure 6 shows the permeability structure along a vertical slice encompassing
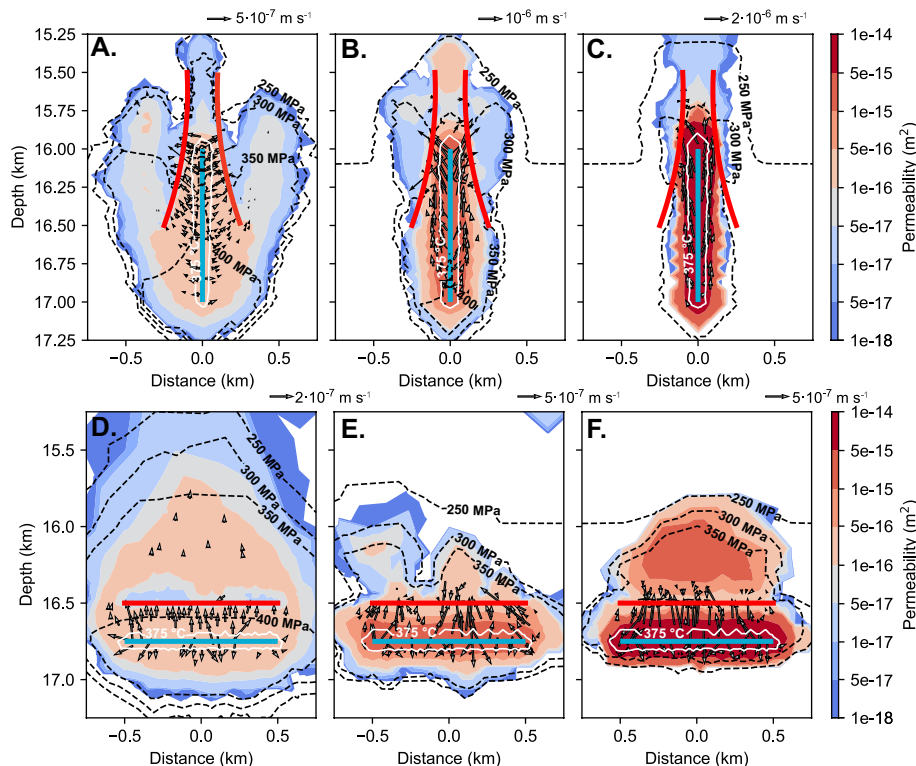

Fig. 6 The permeability structure around a **A**–**C** vertically or **D**–**F** horizontally oriented NDR-EGS after 1 year of fluid circulation. Areas corresponding to the stimulated volume ($> 10^{-16}$ m^2) are shaded in red. Results are shown for maximum permeability increase of **A**, **D** two, **B**, **E** three, or **C**, **F** four orders of magnitude permeability increase relative to the background depth-dependent permeability, corresponding to maximum permeability of **A**, **D** $\sim 10^{-16}$ m^2, **B**, **E** $\sim 10^{-15}$ m^2, or **C**, **F** $\sim 10^{-14}$ m^2. Black dashed lines show isobars and the white line the 375 ℃ isotherm. Rock with permeability less than 10^{-18} m^2 is shown in white and represents the unstimulated part of the domain

the plane of the vertically oriented triplet (Fig. 6a–c) and horizontally oriented doublet (Fig. 6d–f), comparing simulations with maximum permeability of $\sim 10^{-16}$ m^2 (Fig. 3a, d), $\sim 10^{-15}$ m^2 (Fig. 3b, e) and $\sim 10^{-14}$ m^2 (c, f) after 1 year of production. The SV is shaded in red colors in Fig. 6 and includes the domain with permeability values $> 10^{-16}$ m^2 as defined above. Figure 6 shows that there is an inverse relationship between the permeability and size of the stimulated volume. If the maximum permeability in the SV is $\sim 10^{-16}$ m^2 (Fig. 6a), the stimulated volume extends over a larger region (up to 0.5 km away from the injector), with an extensive area featuring fluid pressures > 350 MPa. This indicates that the production intervals fail to adequately depressurize the SV due to its low permeability. In contrast, if maximum permeability is $\sim 10^{-15}$ (Fig. 6b) or 10^{-14} m^2 (Fig. 6c), a vertically oriented NDR-EGS develops a narrow SV with elevated fluid pressures confined to the area near the injector. While horizontally oriented injection intervals (Fig. 6d–f) tend to produce a larger stimulated volume, permeability decreases near the production intervals as the injected fluid depressurizes and flows towards the production intervals.

While high fluid pressures are necessary to maintain permeability in the SV during early stages (Fig. 6), at longer timescales the SV is confined to the region that has cooled to brittle conditions ($\sigma_{\mathrm{diff,brittle}} < \sigma_{\mathrm{diff,ductile}}$), which enables the rock to retain permeability at lower fluid pressures (Fig. 2). Figure 7 shows the long-term evolution of permeability around a vertically oriented (Fig. 7a–c) and horizontally oriented (Fig. 7d–f) NDR-EGS with maximum permeability of $\sim 10^{-15}$ m^2 in the SV. After 10 years of fluid
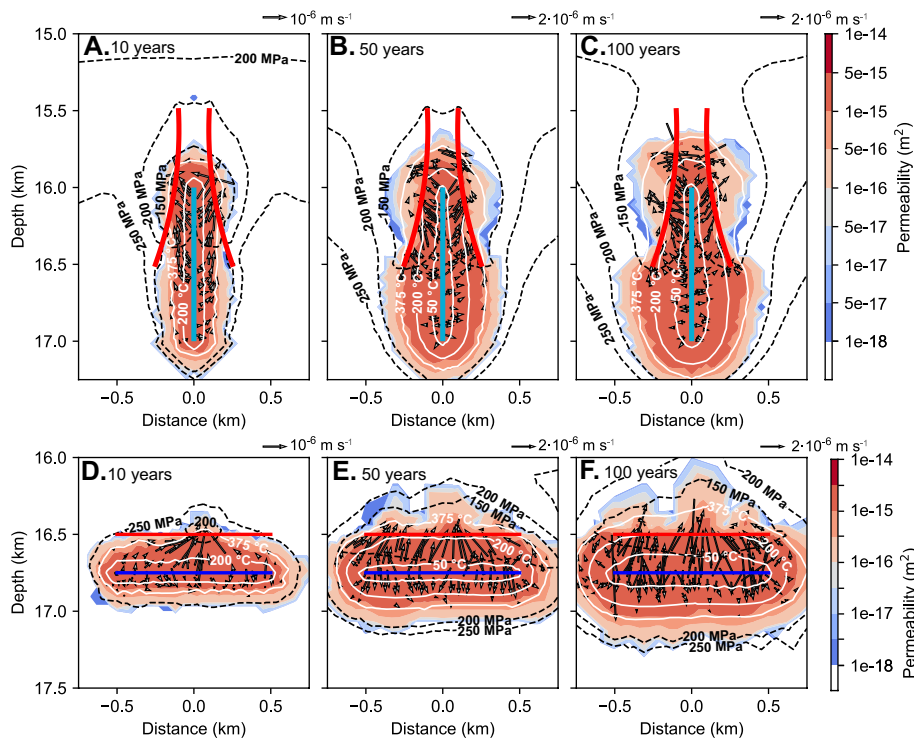

Fig. 7 The permeability structure around a **A–C** vertically or **D–F** horizontally oriented NDR-EGS after **A, D** 10, **B, E** 50, or **C, F** 100 years. Black dashed lines show isobars. White lines show isotherms. Rock with permeability less than 10^{-18} m^2 shown in white

circulation, the SV is nearly entirely confined to the region that has cooled below 375 °C. In comparison to Fig. 6, fluid pressures in the SV are much lower (150–200 MPa), approximately corresponding to the brittle failure pressure of the rock. In the vertically oriented system, continued injection causes the SV to gradually expand laterally below the injection intervals, and the production intervals intercept a larger portion of the stimulated volume with continued injection (Fig. 7b, c). While downward growth of the stimulated volume dominates in a vertically oriented system, the SV expands both laterally away from the injector as well as to greater depths in the horizontally oriented system (Fig. 7d–f). Due to the ability of the system to progressively mine heat from rock at greater distances from the injector, fluid temperatures at the production interval decrease slowly, and are maintained at ∼ 200 °C after 100 years of production (Fig. 7d, f). Moreover, as the SV is a cooler brittle domain embedded in hot, low-permeability, ductile rock, pressurization of the SV does not risk failure of the surrounding rock, as evident by the lack of elevated fluid pressures at 15 km depth above the vertically oriented NDR-EGS (Fig. 7a–c).

The influence of maximum bulk permeability on reservoir evolution

We can divide the operational lifetime of a NDR-EGS into three phases: (1) a stimulation phase, (2) a ductile production phase when high injection pressures are required to maintain permeability in ductile rock, and (3) an extended production phase where fluid injection has cooled the entire SV below the brittle–ductile threshold. Example simulation results showing the evolution of the size and temperature of the stimulated volume over a 100-year operational lifetime are shown in Fig. 8 a, b for different maximum permeability scenarios. During the first ∼ 20 days of stimulation, the SV is relatively small (∼ 10^6 m^3), limited to rock which has cooled to ∼ 300 °C in the immediate vicinity of the injector. Once injection has pressurized the surrounding rock to the failure pressure, the SV begins to grow rapidly. After ∼ 50 days of injection, the stimulated volume has grown to ∼ 10^8 m^3, close to the maximum value before continued injection risks triggering rock failure in the brittle upper crust.

The pressures shown in Fig. 8c are calculated fluid pressures along the injection interval, rather than the calculated well pressures from the Peaceman model. The latter are considerably higher than the fluid and reservoir pressure of the model, whereas the former remain close to the failure pressure as a result of our parameterization. Arguably, injection pressures should not exceed the failure criterion, because rock will hydraulically fracture at this value. Hence, the rate-controlled formulation of the Peaceman model is not directly applicable if well pressure exceeds the failure criterion. Any further pressure increase would lead to displacement (e.g., fracture aperture increase, pore space dilation) within the rock mass surrounding the well, which is not explicitly modeled here. Estimates for fluid pressure are likely better represented by the failure criterion (indicated by the grey lines in Fig. 8c), while the difference between calculated and capped well pressure values may serve as an indicator for the expected degree of damage adjacent to the injection well.

Activating the production wells depressurizes the stimulated volume (Fig. 8c) and briefly causes it to contract around the injector to ∼ 10^7 m^3. With continued injection, however, the stimulated volume grows and maintains a near-constant volume of around
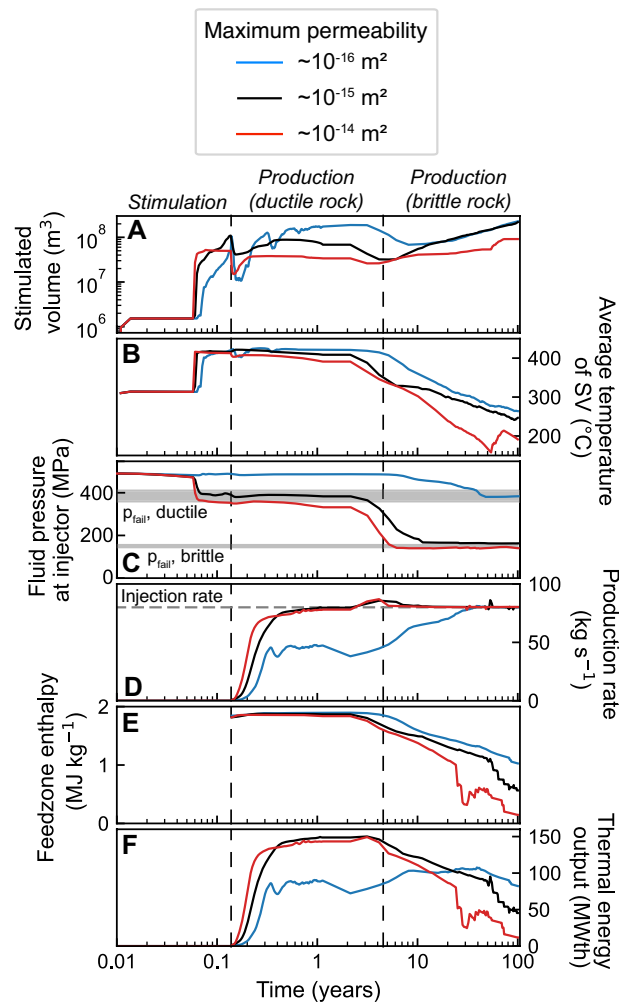
Fig. 8 Heat extraction in NDR-EGS over an operational lifetime of 100 years, showing the **A** size of the stimulated volume; **B** average temperature of the stimulated volume (SV); **C** average fluid pressure along the injection interval; **D** production rate; **E** mass-weighted average feedzone enthalpy; and **F** thermal energy output (MWth), calculated by multiplying the mass flow rate and the specific enthalpy. Grey bars in **C** show the brittle failure criterion, ductile failure criterion, and lithostatic pressure range at the depth of the modeled NDR-EGS system

5×10^7–10^8 m³. The size of the SV starts to grow after ~5 years of production, once its average temperature decreases below ~400 °C. Along with the decrease in the injection pressure (Fig. 8c), this signals the transition from a SV controlled by ductile failure mechanisms to a SV controlled by brittle failure mechanisms. Continued cooling of the SV results in more gradual expansion, and temperatures >200 °C persist throughout the SV even after ~100 years of fluid circulation. Note that while the temperature histories given in Fig. 8b reflect the average temperature of the SV, feedzone enthalpy shown in Fig. 8f is calculated as a mass-weighted enthalpy for the entire production interval. Transient increases in feedzone enthalpy at later times (>50 years) result from the expansion of the SV due to cooling that enables heat extraction from a larger rock volume. In contrast, transient decreases in feedzone enthalpy reflect the development of preferential flow pathways between the injection and production interval.

The permeability of the SV is the main control on the efficiency of heat extraction and the rate of temperature decrease. In our models, we vary the maximum permeability after rock failure to two, three or four orders of magnitude above the initial depth- and temperature-dependent value, corresponding to maximum permeability of $\sim 10^{-16}$, $\sim 10^{-15}$, or $\sim 10^{-14}$ m^2. If the maximum permeability of the SV is low ($\sim 10^{-16}$ m^2), the SV is larger (blue lines; Fig. 8a) and maintains higher temperatures (Fig. 8b), but the power generation potential at earlier times is lower (Fig. 8d and f) and the required injection pressures are extremely high, in excess of the failure pressure for ductile rock (Fig. 8c). High permeability ($> 10^{-14}$ m^2) in the stimulated volume allows efficient heat extraction from the rock (red lines; Fig. 8f) but results in smaller stimulated volumes (Fig. 8a) that cool more rapidly (Fig. 8c). A balance between the size and rate of temperature decrease is achieved when permeability within the SV is $\sim 10^{-15}$ m^2, resulting in a higher long-term power generation potential (black lines; Fig. 8f).

Estimates of thermal energy output

The thermal energy output of these systems depends on the mass flow rate and specific enthalpy of fluid flowing into the production interval (Fig. 8d–f). During the ductile production phase, thermal energy output is as high as ~ 150 MWth if the permeability of the SV is $\sim 10^{-15}$–10^{-14} m^2. If permeability is 10^{-16} m^2, the production rate is lower, because not all the injected fluid reaches the production intervals (Fig. 8d). Throughout the brittle production phase, thermal energy output remains near constant (~ 80 MWth) if the permeability of the stimulated volume is 10^{-16} m^2, but decreases steadily if permeability is $\sim 10^{-14}$–10^{-15} m^2 (Fig. 8f), reflecting the decreasing specific enthalpy of the fluid flowing into the well (Fig. 8e). Thermal energy output decreases to ~ 10 MWth after 30 years if the permeability of the stimulated volume is $\sim 10^{-14}$ m^2, but thermal energy production > 100 MWth persists for ~ 20 years if the permeability of the stimulated volume is $\sim 10^{-15}$ m^2. The decline rate is gradual, with production temperatures and thermal energy output exceeding 250 °C and > 40 MWth, respectively, for ~ 100 years of operation.

We now consider the influence of well configuration, injection rate, and permeability on power generation potential and injection pressure. Over the first ~ 20 years of operation, the highest thermal energy output is observed in systems with maximum permeability of 10^{-15}–10^{-14} m^2. Relative to vertically oriented wells (circles in Fig. 9), horizontally oriented wells (stars) result in slightly higher average thermal energy output (~ 125 MWth), particularly if the permeability of the SV is 10^{-14} m^2. The thermal energy output of systems with lower permeability (10^{-16} m^2) in the SV is lower (< 100 MWth) and the modeled long-term fluid pressures along the injection interval reach much higher values (~ 550 MPa), which likely cannot be realized in practice. Although our well model calculates injection pressures in excess of the failure criterion (Fig. 6c), this is unlikely, as such pressures would introduce failure and permeability enhancement (hydraulic fracturing), which would decrease fluid pressures at the injector.

If the injection rate is lower (~ 40 kg s^{-1}, triangles in Fig. 9), the thermal energy output is also lower (~ 50–60 MWth), but the injection pressure is similar if maximum permeability in the SV is 10^{-15}–10^{-14} m^2. The minimum fluid pressure differential between the injector and producer is governed by the brittle failure criterion and the
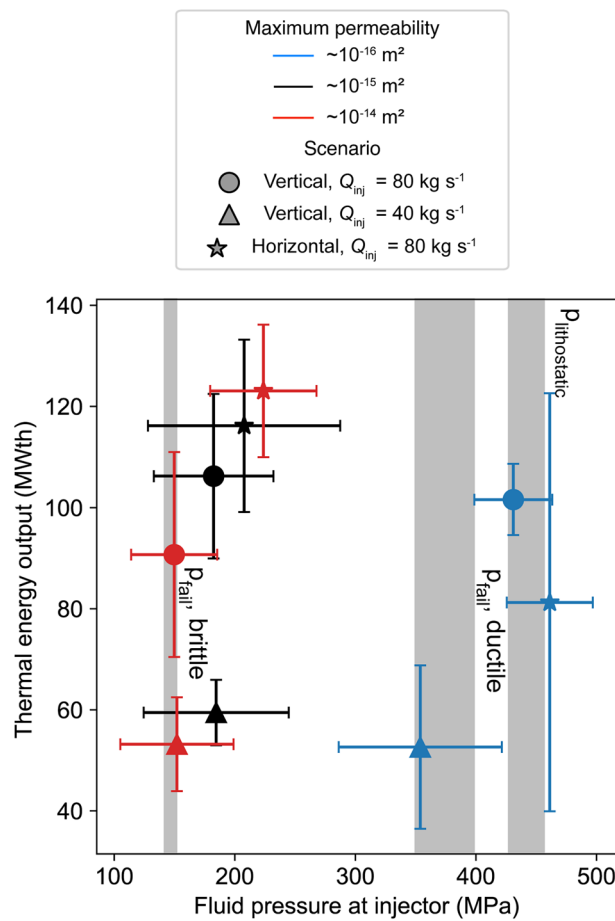
Fig. 9 Average thermal energy output and injection pressure for different NDR-EGS operational scenarios with vertical (circles, triangles) or horizontal (stars) production/injection intervals, injection rate (Q_{inj}) of 40 (triangles) or 80 (circles, stars) kg s^{-1}, and maximum permeability (k_{max}) of 10^{-16} (blue), 10^{-15} (black), and 10^{-14} (red) m^2 in the stimulated volume. Error bars show two standard deviations averaged over the first 20 years of operational lifetime. Grey bars show the brittle failure criterion, ductile failure criterion, and lithostatic pressure range at the depth of the modeled NDR-EGS system. Injection pressures in excess of the ductile failure criterion or lithostatic pressure indicate inadequate permeability increase in the stimulated volume

flowing bottomhole pressure. The thermal energy output is ultimately limited by injection rate, and higher permeability ($> 10^{-14}$ m^2) can result in lower thermal energy output due to more rapid thermal drawdown of the SV (Fig. 8). Based on these results, we conclude that optimal permeability in the SV is 10^{-15}–10^{-14} m^2.

Discussion

Modeled constraints on power production potential

Power production from nominally ductile rock enhanced geothermal systems (NDR-EGS) can be estimated by multiplying the thermal energy output by a conversion efficiency describing the ratio of net electric power generated (MWe) to the heat extracted from the reservoir (MWth). The conversion efficiency in conventional geothermal power generation is approximately 0.1–0.2, with the higher value representing wells that discharge pure vapor (Zarrouk and Moon 2014). Figure 9 shows

that the thermal energy output of a system circulating 80 kg s^{-1} through $\sim$ 425 ℃ rock reaches up to 120–140 MWth. Assuming a conversion efficiency of 0.15, we calculate that the theoretical power generation potential for these systems is $\sim$ 20 MWe. This calculation assumes a conservative conversion efficiency because increasing pressure decreases the specific enthalpy of water. If the fluid ascends near-adiabatically in the wellbore, it will be at two-phase conditions near the surface, given that the specific enthalpy of water flowing into the production interval is approximately 1.9 MJ kg^{-1} (Fig. 8e). The theoretical power generation potential is lower than the output of wells that tap supercritical reservoir fluids near shallow magmatic intrusions (up to $\sim$ 36 MWe; Axelsson et al. 2014), and discharge single-phase vapor. However, our models suggest that the short-term ($<$ 20 years) theoretical power generation per unit mass fluid circulated in a NDR-EGS system is approximately five times greater than that of conventional EGS systems with temperatures of 200 ℃ ($\sim$ 0.25 MWe kg^{-1} s^{-1} compared to $\sim$ 0.05 MWe kg^{-1} s^{-1}; Tester et al. 2006).

To assess power generation possibilities, one can also calculate the power density, which is defined as the average power generation per unit of land surface area required for operation (Smil 2015). Assuming a surface footprint of approximately 0.1 km^2 for the well-pad hosting the simulated doublet system, our simulations suggest that the power density of NDR-EGS is 100–200 W m^{-2}, which is comparable to high-grade oil and gas resources (Smil 2015). Based on these values, we can estimate that approximately 3000 km^2 (an area of roughly 55×55 km^2) would be required to supply the entire electricity demand of the USA in 2022 ($\sim$ 4 TWh).

Further considerations on rock behavior

Our numerical models are subject to several limitations and uncertainties. The models use a continuum porous media approach and assume rock–fluid thermal equilibrium. While this assumption is likely invalid for conventional EGS in which flow is restricted to fractures, experimental evidence suggests that fluid injection in nominally ductile rock generates microfracture networks (Watanabe et al. 2017, 2019, 2020; Goto et al. 2021, 2023). Such "cloud-fracture" networks could provide more uniformly distributed permeability, allowing injected fluid to diffuse into the hot rock surrounding the injection well, and enhancing fluid–rock thermal equilibrium. As our models imply an extended production phase in brittle rock, this may reintroduce the risk of short-circuiting, as in conventional EGS, unless such behavior is forestalled by the development of microfracture networks or the higher confining pressures. However, our model does not explicitly model the stress state. Instead, we invoke a simplified relationship between differential stress and rock failure pressure (Eq. 8), as depicted in Fig. 1d. We also assume idealized and uniform rock properties and behavior, and consider the physics of thermal cracking in a simplified manner.

Our model assumes that failure of ductile rock requires high fluid pressures due to the lower differential stress. However, experimental studies of injection into rock at temperatures of $\sim$ 450 °C with lower confining pressures ($\sim$ 50 MPa) suggest that the failure pressure can be described by the Griffith brittle failure criterion, similar to Eq. 8 (Watanabe et al. 2019, 2020; Goto et al. 2021, 2023). Although the strain rates of deformational experiments in laboratory settings (10^{-5} s^{-1}; Violay et al. 2012; Violay

et al. 2015; Zoback et al. 2002) are more than ten orders of magnitude greater than the background strain rate found in continental crust (10^{-19}–10^{-17} s^{-1}; Zoback and Townend 2001), causing the brittle–ductile transition temperature to be elevated in laboratory settings, elevated strain rates are likely to be attained in the vicinity of a deep injection well in nominally ductile rock. We may be overestimating the temperature of the brittle–ductile transition by assuming a constant strain rate of 10^{-15} s^{-1}, causing our rock failure pressure and injection pressure to be similarly overestimated. We assume that rock permeability can be retained at fluid pressures only slightly in excess of hydrostatic in cooled nominally ductile rock, and that fluid can circulate through the cooled stimulated volume at pressures well below the failure pressure of the surrounding rock. Factors that could contribute to permeability loss over time include fluid–rock interaction and ductile deformation of thermally induced microfractures (Watanabe et al. 2020; Moore et al. 1994). Lastly, as we assume an over-pressured lower crust with a finite porosity (Fig. 1), our model deviates from the conceptual model of a dry lower crust with essentially zero porosity (Yardley 2009).

These uncertainties largely reflect the reality that the time- and path-dependence of rock permeability is not well constrained at pressure and temperature conditions representative of NDR-EGS. In nature, rock is heterogeneous, with variations in properties, stress states, strain rates and pre-existing fractures and fault zones. Direct in situ measurements of permeability are rare at depths >2–3 km (Ingebritsen and Manning 1999) and non-existent below 12 km depth, and even laboratory measurements of permeability are rare at temperatures representative of NDR-EGS (Meyer et al. 2023). Our models illustrate the need for additional research addressing (i) the dominant mechanisms of permeability creation and destruction, and (ii) fluid flow dynamics at fine spatial scales and protracted temporal scales. Further, accurately quantifying the power generation potential from these types of systems will require explicitly modeling fluid ascent in the wellbore (e.g., Lamy-Chappuis et al. 2022).

The presented simulations capture the first-order hydrologic constraints governing these systems, and in particular the need for bulk permeability of 10^{-15}–10^{-14} m^2 in the stimulated volume. Various observations and theoretical limitations constrain large-scale permeability values in ductile crust during regional metamorphism and fault zone fluid-driven processes to $\sim 10^{-16}$ m^2 (Manning and Ingebritsen 1999; Ingebritsen and Manning 2010; Townend and Zoback 2000). This value is two to four orders of magnitude above values commonly measured in the laboratory on centimeter-scale rock samples at ductile conditions (Noël et al. 2021; Petrini et al. 2021; Meyer et al. 2023), and two orders of magnitude above the maximum estimated permeability during regional metamorphism and fault zone fluid-driven processes (Ingebritsen and Manning 2010). However, bulk km-scale permeability at depth is generally one to two orders of magnitude higher than that measured in the laboratory (Townend and Zoback 2000; Zoback and Townend 2001). Moreover, permeabilities as high as $\sim 10^{-14}$–10^{-15} m^2 have been inferred at depths of ~ 35 km due to fluid migration during a seismic event (Nippress and Rietbrock 2007). However, for reasons detailed in, e.g., Ingebritsen and Manning (2010), these earthquake-associated permeability increases are likely local and transient.

Drilling challenges and advanced technologies

Unlocking deep NDR-EGS resources presents a formidable challenge, primarily stemming from the limitations of conventional drilling methods. As mentioned in the Introduction, new drilling technologies have been proposed that replace the mechanical tools, electronics, and drilling fluids with novel drilling processes and downhole equipment less susceptible to failure from the extreme conditions downhole. Millimeter Wave drilling (Oglesby et al. 2014; Houde et al. 2021; Zhang et al. 2023) and plasma-bit drilling (Kocis et al. 2015) are two "energy-based" drilling methods that utilize rapid heating to induce failure or phase change in the rock that reduces it to cuttings that can be conveyed uphole via circulating drilling fluids. Spallation drilling (Beentjes et al. 2019; Kant et al. 2017; Rossi et al. 2020; Holtzman et al. 2023) also destroys the rock without requiring mechanical tools to physically contact the rock, inducing wear. However, the practical application and effectiveness of these innovative drilling techniques have yet to be tested under the extreme downhole conditions characteristic of the depths discussed in this study.

Completion of these wells is another challenge for drilling through hard and hot ductile rock. Novel drilling technologies must prevent ductile deformation into the borehole at the drilling front and may also require casing-while-drilling capabilities that can prevent borehole collapse in the weakened ductile region, whether lining the hole with high-temperature metal casing or other additive materials that prevent ductile failure and creep into the borehole.

Conclusions

It has long been recognized that low-permeability, hot rock can be a significant source of zero-carbon, baseload electricity. Currently, projects investigating the feasibility of drilling into rock at supercritical temperatures near shallow, upper crustal intrusions are ongoing in Japan (Asanuma et al. 2021), New Zealand (Chambefort 2023), the United States (Cladouhos and Callahan 2023) and Iceland (Eichelberger et al. 2021). Our simulations of nominally ductile rock enhanced geothermal systems (NDR-EGS) emphasize the potential resources with temperatures in excess of 400 °C that exist at depths greater than 10–20 km anywhere on the planet. Our models highlight the dynamic permeability response of NDR as the stimulated volume transitions from dominantly ductile to brittle behavior with increased cooling. Intermediate permeability (10^{-15}–10^{-14} m^2) in the stimulated volume is required to achieve practical injection pressures and ensure sustained thermal energy output of ~100 MWth for up to two decades and production temperatures >250 °C for up to a century. As the stimulated volume cools and facilitates fluid circulation at lower absolute pressures than the failure pressure of surrounding ductile crust, our simulations suggest that the stimulated volume of NDR-EGS can be effectively isolated from the overlying critically stressed crust, mitigating the risk of induced seismicity. Higher permeability in the stimulated volume results in a more rapid drop in production temperatures due to increased channeling of injected fluid into high permeability conduits. Horizontal injection intervals can stimulate a more laterally extensive rock volume, slowing the rate of temperature decrease at production wells.

Our modeled systems could attain power generation potentials of ~ 20 MWe (comparable to magma-related geothermal systems in the shallow, brittle crust) and power densities of $100{-}200$ W m^{-2} (comparable to oil and gas reservoirs). These rough estimates naturally have large uncertainties but can nevertheless support further research into NDR-EGS as a potential contributor to a decarbonized energy system, provided that their operation becomes technologically feasible and economic in the future.

The potential of these kinds of geothermal resources depends on the ability for hydraulic or other stimulation technologies to enable transiently higher permeabilities in the ductile crust than arise from natural processes, except over short timescales like seismic events. Integration of interdisciplinary research and collaboration between academia, industry, and government agencies will be critical to the success of future deep EGS projects.

Abbreviations
EGS   Enhanced geothermal systems
NDR-EGS   Nominally ductile rock enhanced geothermal systems
SV   Stimulated volume

Availability of data and materials
The study uses the software CSMP++ and the algebraic multi-grid solver SAMG, which are subject to licensing via https://mineralsystems.ethz.ch/software/csmp.html and https://www.scai.fraunhofer.de/de/geschaeftsfelder/schnelle-loeser/produkte/samg.html. The necessary information on the numerical method and the simulation setups is provided in the methods section and the references therein (Weis et al. 2012, 2014; Yapparova et al. 2022, 2023).

Declarations

Competing interests
Matthew Houde is employed by a company (Quaise Energy) seeking to develop deep drilling technology. This company financially supported the first author (Samuel Scott) during completion of this research.

References
Armstead HCH, Tester JW. Heat mining. New York: Methuen Inc.; 1987.
Asanuma H, Mogi T, Tsuchiya N, Watanabe N, Naganawa S, Ogawa Y, et al. Japanese supercritical geothermal project for drastic increase of geothermal power generation in 2050. In: Proceedings World Geothermal Congress 2020+1. 2021.
Axelsson G, Egilson T, Gylfadóttir S. Modelling of temperature conditions near the bottom of well IDDP-1 in Krafla, Northeast Iceland. Geothermics. 2014;49:49–57. https://doi.org/10.1016/j.geothermics.2013.05.003.
Bailey RC. Trapping of aqueous fluids in the deep crust. Geophys Res Lett. 1990;17:1129–32. https://doi.org/10.1029/GL017i008p01129.
Beentjes I, Bender JT, Tester JW. Dissolution and thermal spallation of barre granite using pure water hydrothermal jets. Rock Mech Rock Eng. 2019;52:1339–52. https://doi.org/10.1007/s00603-018-1647-2.
Behr WM, Platt JP. Brittle faults are weak, yet the ductile middle crust is strong: implications for lithospheric mechanics. Geophys Res Lett. 2014;41:8067–75. https://doi.org/10.1002/2014GL061349.
Bödvarsson GS, Tsang C-F. Injection and thermal breakthrough in fractured geothermal reservoirs. J Geophys Res. 1982;87:1031–48. https://doi.org/10.1029/JB087iB02p01031.

Brace WF, Kohlstedt DL. Limits on lithospheric stress imposed by laboratory experiments. J Geophys Res. 1980;85(B11):6248–52. https://doi.org/10.1029/JB085iB11p06248.

Brown D, DuTeaux R, Kruger P, Swenson D, Yamaguchi T. Fluid circulation and heat extraction from engineered geothermal reservoirs. Geothermics. 1999;28:553–72. https://doi.org/10.1016/S0375-6505(99)00028-0.

Carter NL, Tsenn MC. Flow properties of continental lithosphere. Tectonophysics. 1987;136:27–63. https://doi.org/10.1016/0040-1951(87)90333-7.

Chambefort, I. Geothermal: The Next Generation—Advancing the understanding of New Zealand's supercritical resources. In: Proceedings World Geothermal Congress 2023. 2023.

Chen W-P, Molnar P. Focal depths of intracontinental and intraplate earthquakes and their implications for the thermal and mechanical properties of the lithosphere. J Geophys Res. 1983;88(B5):4183–214. https://doi.org/10.1029/JB088iB05p04183.

Cladouhos, TT, Callahan, OA. Heat extraction from superhot rock: a survey of methods, challenges, and pathways forward. In: Transactions—Geothermal Resources Council. 2023. pp. 2804–51.

Clauser C, Giese P, Huenges E, Kohl T, Lehmann H, Rybach L, Šafanda J, Wilhelm H, Windloff K, Zoth G. The thermal regime of the crystalline continental crust: Implications from the KTB. J Geophys Res Solid Earth. 1997;102(B8):18417–41. https://doi.org/10.1029/96JB03443.

Coulon CA, Hsieh PA, White R, Lowenstern JB, Ingebritsen SE. Causes of distal volcano-tectonic seismicity inferred from hydrothermal modeling. J Volcanol Geotherm Res. 2017;345:98–108. https://doi.org/10.1016/j.jvolgeores.2017.07.011.

Cox SF. The application of failure mode diagrams for exploring the roles of fluid pressure and stress states in controlling styles of fracture-controlled permeability enhancement in faults and shear zones. Geofluids. 2010;10:217–33. https://doi.org/10.1111/j.1468-8123.2010.00281.x.

Dusseault MB, Bruno MS, Barrera JC. Casing shear: causes, cases, cures. SPE Drill Complet. 2001;16:98–107. https://doi.org/10.2118/72060-PA.

Eichelberger JC, Carrigan C, Ingolfsson HP, Lavallée Y, Ludden J, Markusson S, et al. Magma-sourced geothermal energy and plans for Krafla Magma Testbed, Iceland. In: Proceedings World Geotherm Congress 2020+1. 2021.

Finger JT, Blankenship DA. Handbook of best practices for geothermal drilling. Albuquerque: Sandia National Laboratories; 2010.

Fox DB, Sutter D, Beckers KF, Lukawski MZ, Koch DL, Anderson BJ, et al. Sustainable heat farming: modeling extraction and recovery in discretely fractured geothermal reservoirs. Geothermics. 2013;46:42–54. https://doi.org/10.1016/j.geothermics.2012.09.001.

Friðleifsson GÓ, Elders WA, Albertsson A. The concept of the Iceland deep drilling project. Geothermics. 2014;49:2–8. https://doi.org/10.1016/j.geothermics.2013.03.004.

Frost HJ, Ashby MF. Deformation-mechanism maps for pure iron, two austenitic stainless steels, and a low-alloy ferritic steel. In: Jaffee RI, Wilcox BA, editors. Fundamental aspects of structural alloy design. Boston: Springer US; 1977. p. 27–65.

Garcia J, Hartline C, Walters M, Wright M, Rutqvist J, Dobson PF, et al. The Northwest Geysers EGS demonstration project, California: part 1: characterization and reservoir response to injection. Geothermics. 2016;63:97–119. https://doi.org/10.1016/j.geothermics.2015.08.003.

Gee B, Gracie R, Dusseault MB. Multiscale short-circuiting mechanisms in multiple fracture enhanced geothermal systems. Geothermics. 2021;94:102094. https://doi.org/10.1016/j.geothermics.2021.102094.

Goetze C, Evans B. Stress and temperature in the bending lithosphere as constrained by experimental rock mechanics. Geophys J Int. 1979;59(3):463–78. https://doi.org/10.1111/j.1365-246X.1979.tb02567.x.

Goto R, Watanabe N, Sakaguchi K, Miura T, Chen Y, Ishibashi T, et al. Creating cloud-fracture network by flow-induced microfracturing in superhot geothermal environments. Rock Mech Rock Eng. 2021;54(6):2959–74. https://doi.org/10.1007/s00603-021-02416-z.

Goto R, Nakayama D, Takahashi R, Pramudyo E, Takuma K. Cooling-induced permeability enhancement for networks of microfractures in superhot geothermal environments. Geotherm Energy. 2023;11:7. https://doi.org/10.1186/s40517-023-00251-9.

Grant MA. Physical performance indicators for HDR/EGS projects. Geothermics. 2014;63:2–4. https://doi.org/10.1016/j.geothermics.2015.01.004.

Grigoli F, Cesca S, Rinaldi AP, Manconi A, López-Comino JA, Clinton JF, et al. The November 2017 Mw 5.5 Pohang earthquake: a possible case of induced seismicity in South Korea. Science. 2018;360(6392):1003–6. https://doi.org/10.1126/science.aat2010.

Gringarten AC, Witherspoon PA, Ohnishi Y. Theory of heat extraction from fractured hot dry rock. J Geophys Res. 1975;80(8):1120–4. https://doi.org/10.1029/JB080i008p01120.

Haak V, Hutton R. Electrical resistivity in continental lower crust. Geol Soc London Spec Publ. 1986;24(1):35–49. https://doi.org/10.1144/GSL.SP.1986.024.01.05.

Haar L, Gallagher JS, Kell GS. NBS/NRC steam tables. Washington: Hemisphere; 1984.

Handy MR, Brun JP. Seismicity, structure and strength of the continental lithosphere. Earth Planet Sci Lett. 2004;223:427–41. https://doi.org/10.1016/j.epsl.2004.04.021.

Hayba DO, Ingebritsen SE. Multiphase groundwater flow near cooling plutons. J Geophys Res. 1997;102(B6):12235–52. https://doi.org/10.1029/97JB00552.

Holtzman B, Groebner N, Mittal T, Skarbek R. Quench spallation drilling: a novel head design for routine heat mining above the brittle–ductile transition. In: Proceedings, 48th Workshop on Geothermal Reservoir Engineering. 2023. SGP-TR-224

Houde M, Woskov P, Lee J, Oglesby K, Bigelow T, Garrison G, Uddenberg M, Araque C. Unlocking deep superhot rock resources through millimeter wave drilling technology. In: Transactions—Geothermal Resources Council. 2021. p. 2068–83.

Ingebritsen SE, Manning CE. Geological implications of a permeability-depth curve for the continental crust. Geology. 1999;27(12):1107–10. https://doi.org/10.1130/0091-7613(1999)027%3c1107:GIOAPD%3e2.3.CO;2.

Ingebritsen SE, Manning CE. Permeability of the continental crust: dynamic variations inferred from seismicity and metamorphism. Geofluids. 2010;10:193–205. https://doi.org/10.1111/j.1468-8123.2010.00278.x.

Ingebritsen SE, Sanford W, Neuzil CE. Groundwater in geologic processes. 2nd ed. Cambridge: Cambridge University Press; 2006.

Jackson J. Strength of the continental lithosphere: time to abandon the jelly sandwich? GSA Today. 2002;12(9):4–10. https://doi.org/10.1130/10525173(2002)012%3c0004:SoTCIT%3e2.0.Co;2.

Jones C, Keaney G, Meredith PG, Murrell SAF. Acoustic emission and fluid permeability measurements on thermally cracked rocks. Phys Chem Earth. 1997;22:13–7. https://doi.org/10.1016/s0079-1946(97)00071-2.

Kant MA, Rossi E, Madonna C, Höser D, von Rohr PR. A theory on thermal spalling of rocks with a focus on thermal spallation drilling. J Geophys Res Solid Earth. 2017;122(3):1805–15. https://doi.org/10.1002/2016JB013800.

Kocis I, Kristofic T, Gajdos M, Horvath G, Jankovic S. Utilization of electrical plasma for hard rock drilling and casing milling. SPE/IADC Drill Conf Exhib. 2015. https://doi.org/10.2118/173016-MS.

Kohl T, Mégel T. Predictive modeling of reservoir response to hydraulic stimulations at the European EGS site Soultz-sous-Forêts. Int J Rock Mech Min Sci. 2007;44(8):1118–31. https://doi.org/10.1016/j.ijrmms.2007.07.022.

Kohlstedt DL, Evans B, Mackwell SJ. Strength of the lithosphere: constraints imposed by laboratory experiments. J Geophys Res. 1995;100(B9):17587–602. https://doi.org/10.1007/978-90-481-2642-2_689.

Kozlovsky YA. The world's deepest well. Sci Am. 1984;251:98–105.

Kozlovsky YA. The super deep well of the Kola Peninsula. Springer: New York; 1987.

Kraft T, Deichmann N. High-precision relocation and focal mechanism of the injection-induced seismicity at the Basel EGS. Geothermics. 2014;52:59–73. https://doi.org/10.1016/j.geothermics.2014.05.014.

Lamy-Chappuis B, Yapparova A, Driesner T. Advanced well model for superhot and saline geothermal reservoirs. Geothermics. 2022;105:102529. https://doi.org/10.1016/j.geothermics.2022.102529.

Lehmann F, Reich M, Mezzetti M, Anders E, Voigt M. The future of deep drilling—a drilling system based on electro impulse technology. Oil Gas Eur Mag. 2017;43(4):187–91. https://doi.org/10.19225/171203.

Lukawski MZ, Anderson BJ, Augustine C, Capuano LE, Beckers KF, Livesay B, et al. Cost analysis of oil, gas, and geothermal well drilling. J Pet Sci Eng. 2014;118:1–14. https://doi.org/10.1016/j.petrol.2014.03.012.

Macini P, Mesini E. Rock-bit wear in ultra-hot holes. In: Society of Petroleum Engineers. 1994. pp. 223–30.

Matthai SK, Geiger S, Roberts SG, Paluszny A, Belayneh M, Burri A, et al. Numerical simulation of multi-phase fluid flow in structurally complex reservoirs. Geol Soc Lond Spec Publ. 2007;292(1):405–29. https://doi.org/10.1144/SP292.22.

McClure MW, Horne RN. An investigation of stimulation mechanisms in enhanced geothermal systems. Int J Rock Mech Min Sci. 2014;72:242–60. https://doi.org/10.1016/j.ijrmms.2014.07.011.

Meredith PG, Main IG, Clint OC, Li L. On the threshold of flow in a tight natural rock. Geophys Res Lett. 2012;39(4):1–5. https://doi.org/10.1029/2011GL050649.

Meyer GG, Brantut N, Mitchell TM, Meredith PG. Fault reactivation and strain partitioning across the brittle–ductile transition. Geology. 2019;47(12):1127–30. https://doi.org/10.1130/G46516.1.

Meyer GG, Acosta M, Leclere H, Morier L, Teuscher M, Garrison G, et al. A new high-pressure high-temperature deformation apparatus to study the brittle to ductile transition in rocks A new high-pressure high-temperature deformation apparatus to study the brittle to ductile transition in rocks. Rev Sci Instrum. 2023;94:043903. https://doi.org/10.1063/5.0135947.

Moore DE, Lockner DA, Byerlee JD. Reduction of permeability in granite at elevated temperatures. Science. 1994;265(5178):1558–61. https://doi.org/10.1126/science.265.5178.1558.

Nippress SEJ, Rietbrock A. Seismogenic zone high permeability in the Central Andes inferred from relocations of microearthquakes. Earth Planet Sci Lett. 2007;263(3–4):235–45. https://doi.org/10.1016/j.epsl.2007.08.032.

Noël C, Passelègue FX, Violay M. Brittle faulting of ductile rock induced by pore fluid pressure build-up. J Geophys Res Solid Earth. 2021;126(3):e2020JB021331. https://doi.org/10.1029/2020JB021331.

Norbeck JH, McClure MW, Horne RN. Field observations at the Fenton Hill enhanced geothermal system test site support mixed-mechanism stimulation. Geothermics. 2018;74:135–49. https://doi.org/10.1016/j.geothermics.2018.03.003.

Oglesby KD, Woskov PP, Einstein HH, Livesay B. Deep geothermal drilling using millimeter wave technology (Final Technical Research Report). U.S. Department of Energy Office of EERE—Geothermal Technologies Program. 2014; DE-EE0005504.

Parisio F, Vilarrasa V, Wang W, Kolditz O, Nagel T. The risks of long-term re-injection in supercritical geothermal systems. Nat Commun. 2019;10:4391. https://doi.org/10.1038/s41467-019-12146-0.

Paterson MS, Wong T-F. Experimental rock deformation—the brittle field. New York: Springer Science & Business Media; 2005.

Peaceman DW. Interpretation of well-block pressures in numerical reservoir simulation. Soc Pet Eng J. 1978;18:183–94. https://doi.org/10.2118/6893-PA.

Petrini C, Madonna C, Gerya T. Inversion in the permeability evolution of deforming Westerly granite near the brittle–ductile transition. Sci Rep. 2021;11:1–13. https://doi.org/10.1038/s41598-021-03435-0.

Popov YA, Pevzner SL, Pimenov VP, Romushkevich RA. New geothermal data from the Kola superdeep well SG-3. Tectonophysics. 1999;306(3–4):345–66. https://doi.org/10.1016/S0040-1951(99)00065-7.

Rossi E, Jamali S, Wittig V, Saar MO, von Rohr PR. A combined thermo-mechanical drilling technology for deep geothermal and hard rock reservoirs. Geothermics. 2020;85:101771. https://doi.org/10.1016/j.geothermics.2019.101771.

Rutter EH. On the nomenclature of mode of failure transitions in rocks. Tectonophysics. 1986;122(3–4):381–7. https://doi.org/10.1016/0040-1951(86)90153-8.

Scholz CH. The brittle-plastic transition and the depth of seismic faulting. Geol R. 1988;77:319–28. https://doi.org/10.1007/BF01848693.

Scott S, Driesner T, Weis P. Geologic controls on supercritical geothermal resources above magmatic intrusions. Nat Commun. 2015;6:7837. https://doi.org/10.1038/ncomms8837.

Sibson RH. Continental fault structure and the shallow earthquake source. J Geol Soc London. 1983;140:741–67. https://doi.org/10.1144/gsjgs.140.5.0741.

Sibson RH. The edge of failure: critical stress overpressure states in different tectonic regimes. Geol Soc Lond Spec Publ. 2017;458:131–41. https://doi.org/10.1144/SP458.5.

Sibson RH, Robert F, Poulsen KH. High-angle reverse faults, fluid-pressure cycling, and mesothermal gold-quartz deposits. Geology. 1988;16(6):551–5. https://doi.org/10.1130/0091-7613(1988)016%3c0551:HARFFP%3e2.3.CO;2.

Sillitoe RH. Porphyry copper systems. Econ Geol. 2010;105:3–41. https://doi.org/10.2113/gsecongeo.105.1.3.

Simpson F. Fluid trapping at the brittle–ductile transition re-examined. Geofluids. 2001;1:123–36. https://doi.org/10.1046/j.1468-8123.2001.00011.x.

Siratovich PA, Villeneuve MC, Cole JW, Kennedy BM, Bégué F. Saturated heating and quenching of three crustal rocks and implications for thermal stimulation of permeability in geothermal reservoirs. Int J Rock Mech Min Sci. 2015;80:265–80. https://doi.org/10.1016/j.ijrmms.2015.09.023.

Smil V. Power density: a key to understanding energy sources and uses. Cambridge: The MIT Press; 2015.

Tarasovs S, Ghassemi A. Self-similarity and scaling of thermal shock fractures. Phys Rev E. 2014;90:012403. https://doi.org/10.1103/PhysRevE.90.012403.

Taron J, Elsworth D. Coupled mechanical and chemical processes in engineered geothermal reservoirs with dynamic permeability. Int J Rock Mech Min Sci. 2010;47(8):1339–48. https://doi.org/10.1016/j.ijrmms.2010.08.021.

Tester JW, Anderson B, Batchelor A, Blackwell D, DiPippo R, Drake E, et al. The future of geothermal energy: impact of enhanced geothermal systems (EGS) on the United States in the 21st century. Cambridge: The MIT Press; 2006.

Townend J, Zoback MD. How faulting keeps the crust strong. Geology. 2000;28(5):399–402. https://doi.org/10.1130/0091-7613(2000)028%3c0399:HFKTCS%3e2.3.CO;2.

Tullis J, Yund RA. Experimental deformation of dry westerly granite. J Geophys Res. 1977;82:5705–18. https://doi.org/10.1029/JB082i036p05705.

Vik HS, Salimzadeh S, Nick HM. Heat recovery from multiple-fracture enhanced geothermal systems: the effect of thermoelastic fracture interactions. Renew Energy. 2018;121:606–22. https://doi.org/10.1016/j.renene.2018.01.039.

Violay M, Gibert B, Mainprice D, Evans B, Dautria J-M, Azais P, et al. An experimental study of the brittle–ductile transition of basalt at oceanic crust pressure and temperature conditions. J Geophys Res Solid Earth. 2012;117:B03213. https://doi.org/10.1029/2011JB008884.

Violay M, Gibert B, Mainprice D, Burg J-P. Brittle versus ductile deformation as the main control of the deep fluid circulation in oceanic crust. Geophys Res Lett. 2015. https://doi.org/10.1002/2015GL063437.

Violay M, Heap MJ, Acosta M, Madonna C. Porosity evolution at the brittle–ductile transition in the continental crust: implications for deep hydro-geothermal circulation. Sci Rep. 2017;7(1):7705. https://doi.org/10.1038/s41598-017-08108-5.

Wang X-Q, Schubnel A, Fortin J, Guéguen Y, Ge H-K. Physical properties and brittle strength of thermally cracked granite under confinement. J Geophys Res Solid Earth. 2013;118(12):6099–112. https://doi.org/10.1002/2013JB010340.

Watanabe N, Egawa M, Sakaguchi K, Ishibashi T, Tsuchiya N. Hydraulic fracturing and permeability enhancement in granite from subcritical/brittle to supercritical/ductile conditions. Geophys Res Lett. 2017;44(11):5468–75. https://doi.org/10.1002/2017GL073898.

Watanabe N, Sakaguchi K, Goto R, Miura T, Yamane K, Ishibashi T, et al. Cloud-fracture networks as a means of accessing superhot geothermal energy. Sci Rep. 2019;9:1–11. https://doi.org/10.1038/s41598-018-37634-z.

Watanabe N, Saito K, Okamoto A, Nakamura K, Ishibashi T, Saishu H, et al. Stabilizing and enhancing permeability for sustainable and profitable energy extraction from superhot geothermal environments. Appl Energy. 2020;260:114306. https://doi.org/10.1016/j.apenergy.2019.114306.

Wehrens P, Berger A, Peters M, Spillmann T, Herwegh M. Deformation at the frictional-viscous transition: evidence for cycles of fluid-assisted embrittlement and ductile deformation in the granitoid crust. Tectonophysics. 2016;693:66–84. https://doi.org/10.1016/j.tecto.2016.10.022.

Weis P. The dynamic interplay between saline fluid flow and rock permeability in magmatic-hydrothermal systems. Geofluids. 2015;15:350–71. https://doi.org/10.1111/gfl.12100.

Weis P, Driesner T, Heinrich CA. Porphyry-copper ore shells form at stable pressure-temperature fronts within dynamic fluid plumes. Science. 2012;338(6114):1613–6. https://doi.org/10.1126/science.1225009.

Weis P, Driesner T, Coumou D, Geiger S. Hydrothermal, multiphase convection of H2O-NaCl fluids from ambient to magmatic temperatures: a new numerical scheme and benchmarks for code comparison. Geofluids. 2014;14(3):347–71. https://doi.org/10.1111/gfl.12080.

Whittington AG, Hofmeister AM, Nabelek PI. Temperature-dependent thermal diffusivity of the Earth's crust and implications for magmatism. Nature. 2009;458(7236):319–21. https://doi.org/10.1038/nature07818.

Yapparova A, Lamy-Chappuis B, Scott SW, Driesner T. A Peaceman-type well model for the 3D Control Volume Finite Element Method and numerical simulations of supercritical geothermal resource utilization. Geothermics. 2022;105:102156. https://doi.org/10.1016/j.geothermics.2022.102516.

Yapparova A, Lamy-Chappuis B, Scott SW, Gunnarsson G, Driesner T. Cold water injection near the magmatic heat source can enhance production from high-enthalpy geothermal fields. Geothermics. 2023;112:102744. https://doi.org/10.1016/j.geothermics.2023.102744.

Yardley BWD. The role of water in the evolution of the continental crust. J Geol Soc Lond. 2009;166:585–600. https://doi.org/10.1144/0016-76492008-101.

Yardley BWD, Valley JW. The petrologic case for a dry lower crust. J Geophys Res. 1997;102:12173–85. https://doi.org/10.1029/97JB00508.

Zarrouk SJ, Moon H. Efficiency of geothermal power plants: a worldwide review. Geothermics. 2014;51:142–53. https://doi.org/10.1016/j.geothermics.2013.11.001.

Zhang A, Millmore S, Nikiforakis N. Thermal simulation of millimetre wave ablation of geological materials. Comput Geotech. 2023;161:105571. https://doi.org/10.1016/j.compgeo.2023.105571.

Zoback MD, Harjes H-P. Injection-induced earthquakes and crustal stress at 9 km depth at the KTB deep drilling site, Germany. J Geophys Res Solid Earth. 1997;102(B8):18477–91. https://doi.org/10.1029/96JB02814.

Scott *et al. Geothermal Energy*   *(2024) 12:10*

Page 26 of 26

Zoback MD, Townend J. Implications of hydrostatic pore pressures and high crustal strength for the deformation of intra-plate lithosphere. Tectonophysics. 2001;336:19–30. https://doi.org/10.1016/S0040-1951(01)00091-9.

Zoback MD, Townend J, Grollimund B. Steady-state failure equilibrium and deformation of intraplate lithosphere. Int Geol Rev. 2002;44:383–401. https://doi.org/10.2747/0020-6814.44.5.383.

Publisher's Note